Bi-$MoSe_2$ contacts in the ultraclean limit: closing the theory-experiment loop

Yang Liu[1#], Song Liu[2#], Zhiying Wang[2#], Ashraf Hasan Mohammad Al-bqerat[3], Amirali Zangiabadi[4], Vasili Perebeinos[3*], James Hone[2*]*

[1]Key Laboratory for the Physics and Chemistry of Nanodevices, School of Electronics, Peking University, Beijing 100871, China

[2]Department of Mechanical Engineering, Columbia University, New York, NY, USA.

[3]Department of Electrical Engineering, University at Buffalo, Buffalo, NY 14260, USA

[4]Department of Applied Physics and Applied Mathematics, Columbia University, New York, NY, USA.

Email: liuyang.nano@gmail.com, vasilipe@buffalo.edu, jh2228@columbia.edu

Keywords: Ultraclean, transition metal dichalcogenides, contact, defect, model

Abstract: Achieving robust electrical contacts is crucial for the promise of monolayer 2D semiconductors like semiconducting transition metal dichalcogenides (s-TMDs) in electronic technologies. Despite breakthroughs in low contact resistance, a gap remains between experiment and theory, partly due to uncontrolled experimental imperfections. This study

explores bismuth semimetal contacts to monolayer $MoSe_2$, using a platform with ultrahigh-purity MoSe2, damage- and strain-free interfaces, and hBN encapsulation. We combine contact-front and contact-end measurements to measure key parameters like specific resistivity (ρ_c) and transfer length (L_t). We find that the resistivity of $MoSe_2$ under the contacts is 20 times higher than in the channel at room temperature, and even higher at lower temperatures. This result is accurately modeled using a self-consistent approach combining electrostatics and band structure. In contrast, *ab initio* calculations of the interlayer charge transfer rate are inconsistent with the measured value of ρ_c, highlighting the need for new theoretical approaches.

Semiconducting monolayer transition metal dichalcogenides (s-TMDs) have emerged as highly promising materials for electronics and optoelectronics[1,2]. For instance, monolayer s-TMDs can potentially far outperform silicon in deeply scaled CMOS due to superior electrostatic gate control and improved mobility in the ultrathin limit[3-5]. However, achieving low-resistance contacts to monolayer s-TMDs remains a major challenge[6]. Recently, there have been several breakthroughs in reducing contact resistance to monolayer s-TMDs by employing semimetals, such as Bi and Sb, which have low work function and low density of states that can inhibit the formation of metal-induced gap-states[7-10]. Bi- and Sb-contacts to CVD-grown MoS_2 have achieved n-type contact resistance of 123 Ω·μm and 42 Ω·μm, respectively[7,8], which can meet the requirement of the International Roadmap for Devices and Systems (IRDS) 2024 or 2028 targets of logic transistors, respectively. Notably, the underlying

s-TMD is not damaged by the evaporation of these metals, and the metal-s-TMDs interface is atomically abrupt with a clear van der Waals (vdW) gap[11,12]. However, there still exists a lack of fundamental understanding of the contact interfaces, and in particular there is inconsistency between theoretical predictions and experimental demonstration[13]. For instance, the theoretical projection of ultimate performance limit of monolayer MoS_2-based transistor has not yet been realized experimentally[5].

Theoretical modeling of contacts to s-TMDs has almost exclusively considered the idealized situation in which metal contacts are applied to a perfectly crystalline, intrinsic s-TMDs layer[13,14]. However, experiments have been carried out in systems with a high density of defects[12]. These defects have two main origins. First, synthesized s-TMDs (i.e., CVT bulk crystal or CVD monolayer) generally have a large density of point defects – i.e., MoS_2, typically in the range of 10^{13} cm^{-2} (roughly 1% of lattice sites)[15-17]. Second, deposition of metals onto s-TMDs by evaporation can introduce further damage due to the high thermal energy of the deposited metal[18,19]. These external defects strongly modify in-plane transport and introduce in-gap states that lead to Fermi level pinning[18]. Defects can also modify s-TMDs film morphology by partial delimitation of the s-TMDs metal interface, thus increasing the contact resistance and the transfer length (a key parameter to quantify the scaling capability). Thermally activated charged defects can also introduce temperature-dependent doping that can improve in-plane and out-of-plane transport, potentially improving contact resistance[20,21]. As a result of these multiple factors, reported contact resistances show large variability[7]. Finally, because the contacts themselves can strongly perturb the 2D semiconducting layers

beneath, conventional measurement techniques used for bulk semiconductors may not be suitable for characterizing metal-s-TMDs contacts. These previously overlooked factors have made it difficult to 'close the loop' between theory prediction and experimental verification in order to reveal the intrinsic underlying physics within these contacts. A necessary first step toward such 'closed-loop' understanding is to first understand a more idealized case, in which disorder plays a minimal role.

Here, we combine advanced materials synthesis and device assembly to create devices in which the abovementioned sources of disorder and uncertainty are minimized. We utilize high-purity monolayer $MoSe_2$ exfoliated from bulk crystals synthesized through a two-step flux technique[22]. The high-purity monolayer $MoSe_2$ is encapsulated within flakes of hexagonal boron nitride (hBN) to minimize disorder from the surrounding environment. Bismuth contacts are evaporated onto the $MoSe_2$ using a gentle process that does not induce any damage. We first characterize the defect density within the $MoSe_2$ using scanning tunneling microscopy (STM) and then use scanning transmission electron microscopy (STEM) to confirm that the interface between the Bi and $MoSe_2$ is damage- and strain-free. Next, we characterize the Bi-$MoSe_2$ contacts using multi-terminal measurement scheme based on a resistor network model. In the on-state, this model yields contact resistivity ρ_c = 4-5×10^{-6} Ω cm^{-2} and transfer length L_t ~40 nm. The value of L_t is independently verified by my measuring a steep increase in contact resistance when the contact length is below 40 nm. We next seek to develop theoretical understanding of two key aspects of these contacts. First, we observe that the room-

temperature sheet resistance beneath the contact is ~20 times larger than the sheet resistance inside the channel. This ratio and its variation with temperature can be accurately described by a charge transfer model that self-consistently combines electrostatics and band theory. Second, we use density functional theory to calculate charge transfer rates across the junction, and find values that are inconsistent with the measured value of ρ_c. Thus, we can conclude that conventional models can accurately describe charge transfer and band alignment in metal – s-TMD contacts, but not charge transfer rates.

Results

Heterostructure Assembly and Bi-$MoSe_2$ Interface Characterization

We first characterized the quality of the $MoSe_2$ crystals used for exfoliation by examining the surface of a freshly cleaved crystal through STM imaging. Supplementary Figures 1a and 1b shows STM images of the high-purity crystal on different magnification views, indicating an average charged defect density of 5.6×10^9 cm^{-2}. Supplementary Figure 1c shows a typical STS curve with symmetric conduction and valence band edges relative to the Fermi level. All the flakes used for this study were exfoliated from crystals grown in the same ampoule and have a largely similar composition. We can thus conclude that the $MoSe_2$ studied below is an intrinsic (i.e., undoped) semiconductor with an ultra-low defect density-roughly 3-4 orders of magnitude lower than typical CVD-grown s-TMDs[22]. In addition, we utilized Raman and photoluminescence (PL) spectroscopy to confirm the monolayer nature, as shown in Supplementary Figures 1d and 1e.

To assemble polymer-free heterostructures, we designed a three-step process based on a 'flip-chip' technique[23]. First, we identified a suitable (~40 nm thick) top hBN flake and etched slits of desired width through the flake using electron beam lithography (EBL) and reactive ion etching (RIE). Next, we 'flipped' the patterned hBN by picking it up using a polymer, inverting the polymer-hBN stack, and annealing under high vacuum to remove the polymer[23] (Figure 1ai). In this way, a polymer-free surface was exposed upward. Next, we used a second piece of hBN to pick up the monolayer $MoSe_2$ and the flipped etched hBN; the assembled heterostructure was then flipped and annealed under vacuum to remove the supporting polymer (Figure 1aii). Atomic force microscopy (AFM) imaging of the flipped structure (Supplementary Figure 2e) confirm that the slit width can be varied from down to nm range with high uniformity along both *x*- and *y*-direction, and that the surface of the $MoSe_2$ is clean and contamination-free surface after flip-chip annealing. In addition to offering a clean interface, this stacking strategy stabilizes the metal contacts by confining them within the hBN slits. Without this lateral confinement, Bi contacts in the ultra-scaled regime (<100 nm contact length) can easily slide during subsequent processing (Supplementary Figure 2f) since the Bi makes only a van der Waals contact to the $MoSe_2$[11]. Finally, we used EBL to open windows on top of the contact regions and deposited Bi under high vacuum (10^{-8} Torr) by thermal evaporation (Figure 1aiii). Details of the fabrication process can be found in Methods and Supplementary Figures 2a-2d.

We characterized the interface between Bi and $MoSe_2$ using cross-sectional imaging using annular dark field (ADF) scanning transmission electron microscopy (STEM). A cross-sectional image of a structure with monolayer $MoSe_2$ (Supplementary Figure 3) confirms that the Bi-$MoSe_2$ vdW interfaces are intact, with no evidence of damage to the monolayer $MoSe_2$. Further thinning of these structures to the degree required to achieve atomically sharp imaging proven to be very difficult due to separation of the $MoSe_2$ and hBN during processing. Therefore, we examined the interface between Bi and multilayer $MoSe_2$, which was more mechanically robust. Figure 1b shows an atomically-sharp interface with a clear vdW gap between $MoSe_2$ and Bi. To quantify the core-to-core distance between Bi and Se ($d_{Bi\text{-}Se}$), the measured images were simulated using interface geometry shown in Figure 1c. The value of $d_{Bi\text{-}Se}$ was determined to be 2.8 Å by carefully comparing the Nano Electron Diffraction patterns. Furthermore, on the basis of the high-resolution STEM in Fig. 1b, we carried out geometrical phase analysis (GPA) mapping[24], which indicates strain of less than 0.1% at the Bi-$MoSe_2$ interface, as shown in Fig. 1d, and the line plot at the interface depicted in Fig. 1e.

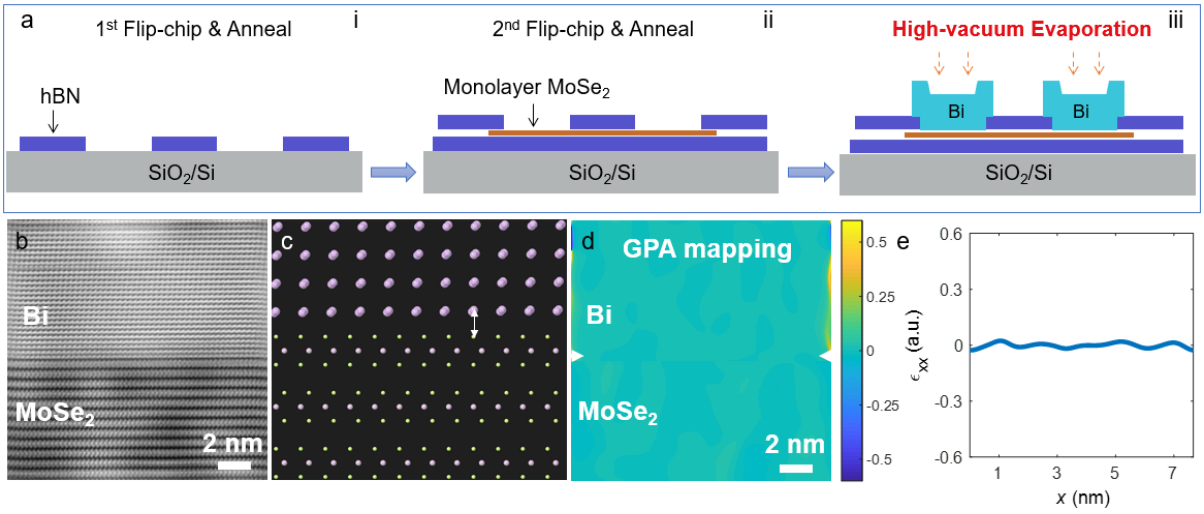

Figure 1. Fabrication flow, atomic resolution imaging and geometrical phase analysis of Bi-$MoSe_2$ interface. a, Fabrication flow of Bi-contacted patterned hBN/monolayer $MoSe_2$/hBN. **b**, Atomic-resolution images of Bi on multilayer $MoSe_2$. **c**, Simulated Bi-$MoSe_2$ heterostructure. **d**, Geometrical phase analysis mapping of the cross-sectional images shown in **b**. **e**, Strain profile along the Bi-$MoSe_2$ interface.

Experimental Characterization of the Bi-$MoSe_2$ Contacts

In this section, we will characterize the carrier transport across the Bi-$MoSe_2$ interface through multi-terminal measurements. Figure 2a depicts the device used to characterize the Bi-$MoSe_2$ contacts, consisting of five separate electrodes spanning an $MoSe_2$ flake with width W = 3.8 μm. Each contact pair was characterized as a field-effect transistor, with the Si wafer acting as a back gate and 285 nm SiO_2 (plus the bottom hBN, ~50 nm thick) as the gate dielectric. The channel length ($L_{chi,}$ i=1, 2, 3, 4) for each pair was 1 μm unless noted otherwise. Contacts A and E are wide (L_{cA}, L_{cE} ~ 1 μm) while contacts B, C, and D are narrow (L_{cB}=75 nm, L_{cC}=60 nm, L_{cD}=40 nm). Supplementary Figure 4 shows room-temperature transfer and output curves for a representative device (corresponding to A and B electrodes in Fig. 2a). The source-drain current (I_{ds}) turns on strongly above gate-source bias of V_{gs}=0 V with a source-drain bias of V_{ds}=0.1 V, behaving like a typical n-type FET.

To determine the properties of the contacts, we measure multi-terminal transport with contacts A and D as drain and source, respectively. For a given source-drain current, the voltage drop between A and D yields the two-terminal resistance R_{2p}; the voltage drop across

electrodes B and C yields the four-terminal resistance R_{4p}, and the voltage measured between electrode D and electrode E yields the contact end resistance R_{ce}. For voltage distribution across the voltage probes B and C (Fig.2a, right panel), we exactly deduced the analytical solution under the current continuous boundary conditions. All device properties are measured at room temperature in the on-state ($V_{gs} > 60$ V) without additional notes.

The on-state behavior of FET contacts is typically described using a transmission line model with three parameters[25]: the sheet resistance of the channel (R_{sh}), the sheet resistance beneath the contacts (R_{sk}), and the contact resistivity (ρ_c) (Fig. 2a, left panel). The combination of R_{sk} and ρ_c determines the transfer length $L_t = \sqrt{\rho_c / R_{sk}}$ that is required for carrier injection and sets the ultimate length scaling limit of side contacts. Likewise, the contact resistance (contact front resistance) for a contact of length L_c is given by $R_{cf} = \frac{\rho_c}{L_t W} \coth(L_c / L_t)$. The commonly used transfer length method (TLM) plots two-terminal resistance vs. channel length to yield R_{cf} from the *y*-intercept and R_{sh} from the slope. L_t is typically determined by extrapolating to find the *x*-intercept. However, this extrapolation assumes that $R_{sk} = R_{sh}$. Such an assumption may not be valid in the 2D limit where the semiconductor can strongly interact with the contact[26]. **Here, we do not assume $R_{sk} = R_{sh}$.**

By modeling the device into a resistor network (detailed analyses are shown in Supplementary Section 10), we find that:

$$R_{4p} = \left(R_{sk} \times \frac{L_t}{W}\right) \times \tanh\left(\frac{L_{cB}}{2L_t}\right) + \left(R_{sk} \times \frac{L_t}{W}\right) \times \tanh\left(\frac{L_{cC}}{2L_t}\right) + R_{sh} \times L_{\mathrm{ch2}}$$

(1)

$$R_{ce} = \left(R_{sk} \times \frac{L_t}{W}\right) / \sinh\left(\frac{L_{cD}}{L_t}\right)$$

(2)

and

$$R_{2p} = \left(2 \times R_{sk} \times \frac{L_t}{W}\right) \times \tanh\left(\frac{L_{cB}}{2L_t}\right) + \left(2 \times R_{sk} \times \frac{L_t}{W}\right) \times \tanh\left(\frac{L_{cC}}{2L_t}\right) + R_{sh} \times (L_{\mathrm{ch1}} + L_{\mathrm{ch2}} + L_{\mathrm{ch3}}) + \left(R_{sk} \times \frac{L_t}{W}\right) \times \coth\left(\frac{L_{cA}}{L_t}\right) + \left(R_{sk} \times \frac{L_t}{W}\right) \times \coth\left(\frac{L_{cD}}{L_t}\right)$$

(3)

From the measured values of R_{2p}, R_{4p}, and R_{ce} (Supplementary Figure 5), these equations can be solved to yield the three independent quantities R_{sk}, R_{sh} and L_t, which can, in turn, be used to calculate R_{cf} and ρ_c. We find R_{cf} =10-16 kΩ · μm, ρ_c=4×10^{-6}-5.5×10^{-6} Ω · cm^2, and L_t=32-38 nm. These quantities are plotted in Figs. 2b-2d. A second device showed comparable values of R_c (Supplementary Figure 6).

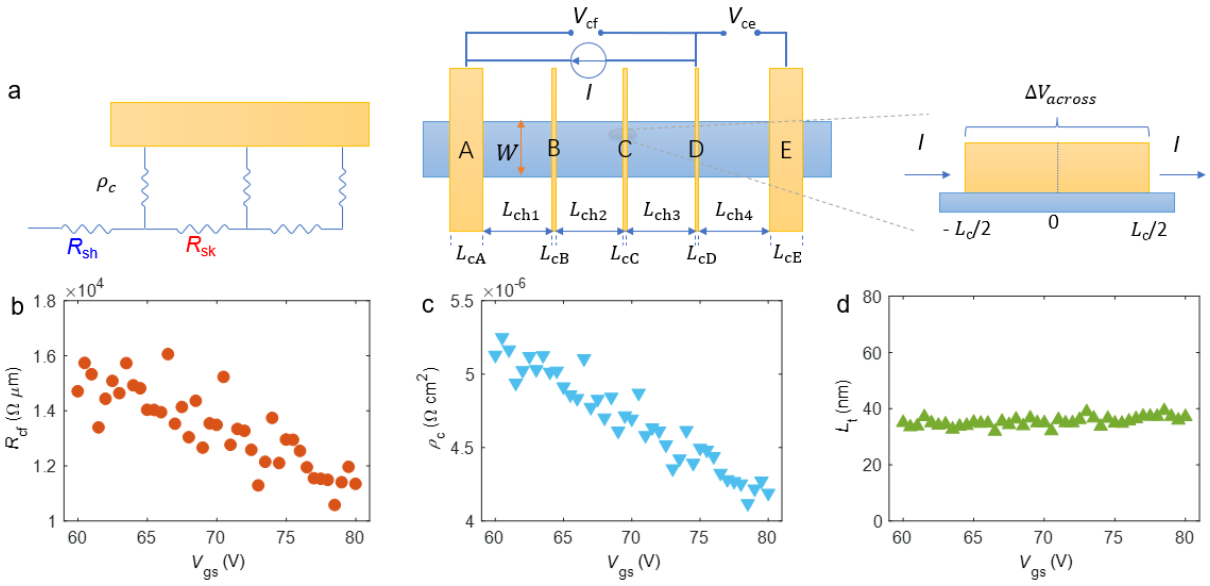

Figure 2. Electrical Characterization of Bi-MoSe2 Contacts. a, Schematics of the measurement configuration consisting of contact-front and contact-end approach. Left panel shows the transmission line model of contacts, where we distinguish the sheet resistance beneath contacts and inside channel. Middle panel is the specific measurement configuration and specific parameter nomination. Contacts B and C are utilized as the four-probe voltage measurement leads. Right panel is the cross-sectional schematics of the voltage distribution across voltage probe B and C. **b-d**, Contact front resistance (R_{cf}), contact resistivity (ρ_c), and transfer length (L_t) as a function of V_{gs}.

Length Scaling of vdW Contacts

The above analysis predicts that both R_{cf} and R_{ce} will increase with decreasing L_c when $L_c \lesssim L_t$. To directly test this prediction, we created another type of device with contact lengths L_c varying from 25 to 75 nm and uniform channel lengths L_{ch} of 1 μm. The size of these contacts

was checked by measuring the width of the slits in the hBN with AFM. Output curves of these devices (Supplementary Figure 8a) confirm that the contacts remain Ohmic even for the shortest lengths, whereas the transconductance (g_m) decreases with decreasing L_c (Supplementary Figure 8b). The 2-terminal resistance R_{2p} of these devices (which includes both contact and channel resistance) at V_{gs}=80 V (Fig. 3a) increases dramatically for L_c< 45 nm, consistent with rapidly increasing R_{cf}. Likewise, R_{ce} also increases with decreasing L_c (Fig. 3b). The length scale corresponding to a 1/e falloff yields a value of L_t ~ 40 nm[25]. This provides essential independent verification of the value of L_t obtained above from the multi-terminal measurements in Figure 2. In particular, the observed scaling shows that effects beyond the resistor network picture, such as tunneling directly from the metal to the channel[27,28], do not play a significant role in the regime studied here.

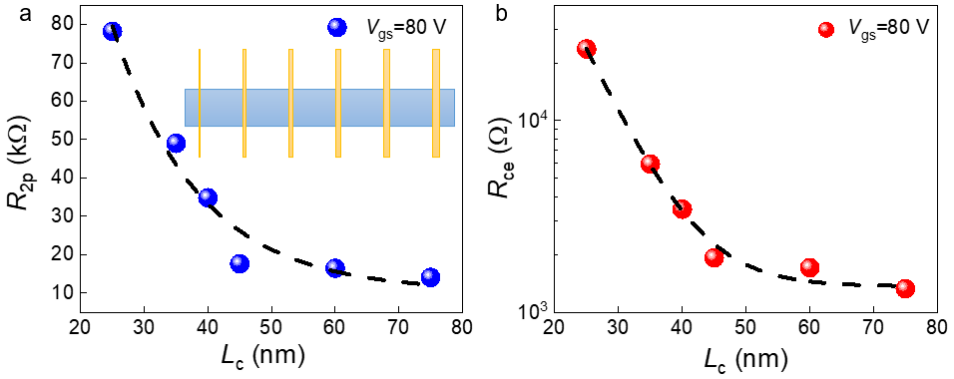

Figure 3. Length scaling of vdW contacts. a-b, R_{2p} (**a**) and R_{ce} (**b**) dependence on L_c at V_{gs}=80 V.

Theoretical Modeling of the Bi-$MoSe_2$ Contacts

Figure 4c shows the derived values of R_{sh} and R_{sk} as a function of V_{gs}. The measured value of $R_{sh} = 1.6 \times 10^4$ Ω/square at $V_{gs} = 80$ V corresponds to electron mobility $\mu \approx 63$ cm^2/Vs (with $n = -c_g (V_{gs} - V_t) = 6.2\times10^{12}$ cm^{-2} using threshold voltage $V_t = -15$ V as determined from the transfer curve, see Supplementary Section 4 and Supplementary Figure 4). The measured mobility is close to the theoretical limit imposed by phonon scattering[29], consistent with the high material quality and low disorder within the heterostructure.

Notably, we find that R_{sk} is roughly 20× greater than R_{sh}. Since the STEM imaging shows no evidence of damage to the $MoSe_2$ by the Bi contact, it is unlikely that excess scattering from defects is responsible for the increased resistance. Likewise, the metal contact should screen fields from charged impurities and polar phonons, thereby reducing scattering beneath the contacts. Therefore, it is likely that the increase in R_{sk} relative to R_{sh} is not due to lower carrier mobility, but instead to decreased carrier density arising from charge transfer between the $MoSe_2$ and the Bi. Therefore, mobilities under the metal in the channel in $MoSe_2$ are assumed to be the same. Below we compare this experimental finding to a model, in which we assume that the entire change in resistance is due to charge transfer, *i.e.* that $n_{ch}/n_c = 20$.

As shown in Figure 4a, this charge transfer can be modeled by self-consistently combining electrostatics and band structure. The carrier density (n_c) of $MoSe_2$ beneath the contacts can be calculated as follows:

$$n_c = -\int_{E_c}^{+\infty} DOSef(E, E_F, T)dE + \int_{-\infty}^{E_v} DOSh(1 - f(E, E_F, T))dE \qquad (4)$$

$$n_c = -c_g\left(V_{gs} - V_{2D}\right) + c_m V_{2D} \qquad (5)$$

where $DOSe = \frac{2m_e}{\pi\hbar^2}$, $DOSh = \frac{2m_h}{\pi\hbar^2}$ are the density of states for electrons and holes, respectively. Note that the effective mass approximation leads to energy-independent density of states in 2D. We use $m_e = m_h = 0.61$ in units of electron mass, as obtained from *ab initio* calculations[30]. Eq. (5) is the solution of the Poisson equation in the planar capacitance model, whereas Eq. (4) represents the equilibrium thermal distribution of electrons with Fermi level E_F and temperature T. The calculations of the composite gate stack capacitance c_g and metal-contact interface capacitance c_m are listed in the Supplementary Information. In order to find E_F as a function of gate voltage, we use the band diagram in Fig. 4a right panel, suggesting $W_m = IF_{2D} + E_c - E_F + eV_{2D}$, where we define $\Delta = W_m - IF_{2D}$ as the difference between Bi work function W_m and s-TMD electron affinity IF_{2D}. We note that this estimate of Δ can only serve as a qualitative estimate and exact value is affected by electron orbital hybridization between the metal and 2D material[31,32] and electron-electron correlations beyond density function theory[33]. Therefore, in our analysis we use Δ as a fitting parameter. At the same time, the charge density on the $MoSe_2$ inside the channel is $n_{ch} = -c_g(V_{gs} - V_{th})$. We neglect quantum capacitance for 50-nm thick h-BN gate insulator.

Next, we solve this model numerically. A self-consistent electrostatics analysis for $n_{ch}/n_c = 20$ yields a band offset of $\Delta = 0.236$ eV, which matches the difference between the work function of Bi (4.23 eV) and the electron affinity of $MoSe_2$ (3.99 eV)[34,35]. It is also consistent with the recent discovery that transferred metal can form Fermi-level-pinning-free contacts with transistion metal dichalcogenides (TMDCs) due to the damage-free interface[19]. The gate-

dependent behavior of R_{sk} and R_{sh} (Figs. 4b and 4c) likewise shows good agreement between experiment and theory, with R_{sk}/R_{sh} staying roughly constant even as both decrease with increasing V_{gs}. Finally, we observe that R_{sk}/R_{sh} increases upon cooling (Fig. 4d and Supplementary Figure 7). This behavior is also reproduced quite well by theory, since the number of carriers from Bi to the $MoSe_2$ is highly T-dependent for positive $\Delta \gg k_B T$, leading to 'source exhaustion'[36]. This convergence further validates the assumption that charge transfer is responsible for the difference between R_{sk} and R_{sh}.

To gain further insight into the microscopic mechanism of vertical transport across Bi and $MoSe_2$, we note that the specific contact resistivity ρ_c can be calculated by considering charge carrier flux across the metal-2D material interface in energy window defined by the voltage difference at the interface eV_i[37,38]. The number of carriers contributing to the current is given by the product of $f \times DOSe \times eV_i$, where $f = 1/(\exp((E_c - E_F)/k_b T) + 1)$ is the carrier population number at the edge of the conduction band. Therefore, ρ_c can be calculated as: $1/\rho_c = I/V_i = e^2 DOSef/\tau_m$, where τ_m is the s-TMDs-metal scattering time, which measures the average time for electron transfer across the interface. τ_m is determined by the strength of the electron orbital hybridization at the interface[39], and is typically estimated using second order perturbation theory[38]. However, the *ab initio* values[39] of the reported τ_m or corresponding ρ_c are typically orders of magnitude smaller than indicated by measurememnts[38]. It is not well understood whether this discrepancy arises from inaccuracy in the theoretical models or from imperfections in the contact interface.

To gain better insight into vertical transport between Bi and $MoSe_2$, here we derive τ_m from the experimental data. The charge transfer model employed above suggests that under the contact, the Fermi level in the $MoSe_2$ under the metal lies roughly 100 meV below the conduction band edge at the highest gate voltage of 80 V, i.e. $E_c - E_F \approx 100$ meV. Using the measured value of $\rho_c = 4.2 \times 10^{-6}$ Ω cm ^{2}, we can calculate $\tau_m \approx 7 \times 10^{-12}$ s. As an independent check of this value, we note that, in the absence of carrier scattering within the $MoSe_2$, electrons will travel a distance $\lambda_m = V_T \times \tau_m \approx 490$ nm before transferring to the metal, where $V_T = (2k_bT/(\pi m_e))^{1/2} \approx 7 \times 10^6$ cm/s is the thermal velocity. The transfer length measured in our experiment is a result of competition between an electron losing its momentum during the scattering process within the $MoSe_2$ and transferring to the metal. As a result $L_t = (\lambda_m \lambda)^{1/2}$, where λ is the in-plane mean free path[38]. Assuming that the mobility beneath the contact is the same as the channel mobility of 63 cm ^{2}/Vs, we calculate $\lambda = V_T \times \tau \approx 1.5$ nm. Therefore, the corresponding transfer length is $L_t = (\lambda_m \lambda)^{1/2} \approx 27$ nm, consistent with the experimental values obtained above.

For direct comparison with this experimental value, we performed *ab initio* calculations of vertical transport through a $MoSe_2$ monolayer sandwiched between two semi-infinite Bi metal slabs. The results (shown in Supplementary Information Section 11 and Supplementary Figure 9) predict a value of ρ_c four orders of magnitude smaller than the experimental value. In this clean system, it is difficult to envision how extrinsic factors at the contact would diminish Bi-$MoSe_2$ coupling by such a large amount. Therefore, this work adds strong support to the idea that microscopic models beyond standard DFT are needed to accurately calculate τ_m. For example, the

mismatch of the Fermi surfaces around the Γ-point in Bi and K-points in $MoSe_2$ due to the lattice mismatch would require momentum relaxation mechanisms such as phonons[40,41], which would increase τ_m and therefore ρ_c.

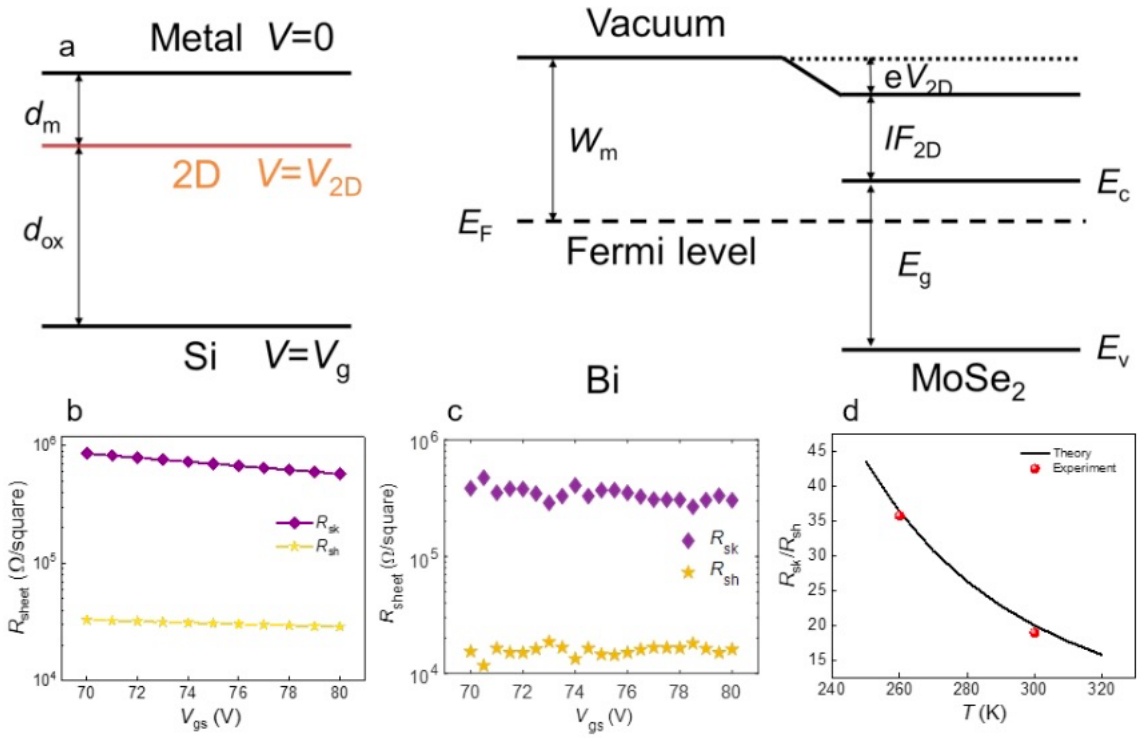

Figure 4. Comparison between model of Bi-$MoSe_2$ charge transfer and experimental data. A, Left panel: Schematics of the contacts geometry used in establishing the electrostatics. Right panel: Energy band diagram. W_m is the metal work function, E_g is the bandgap of monolayer $MoSe_2$, eV_{2D} is the electrostatic potential on $MoSe_2$, IF_{2D} is the electron affinity of monolayer $MoSe_2$. **B-c**, R_{sk} and R_{sh} achieved from the theoretical calculations (**b**) and experimental measurements (**c**). **d**, R_{sk}/R_{sh} versus temperature.

Conclusion

To summarize, we demonstrated a device platform that allows for rigorous testing of metal-vdW contacts and comparison with theory. This heterostructure device features a damage-free and strain-free metal-semiconductor junction with an atomically sharp interface, as confirmed by cross-sectional STEM imaging and geometrical phase analysis. To characterize these devices, we utilized a multi-terminal measurement scheme that is capable of unambiguously determining key metal-semiconductor junction parameters. These measurements indicate transfer length of order 40 nm, a conclusion that is supported by independent observation of a steep increase in contact end resistance with decreasing contact length over the same characteristic length scale. The measurements also show a roughly 20-fold difference between R_{sk} and R_{sh}. In this case, the standard TLM analysis will over-estimate L_t by a factor $\sqrt{\frac{R_{sk}}{R_{sh}}}$, or roughly 4.5. This detailed experimental analysis, combined with the clean experimental system, allows us to begin to close the loop between experiment and theory for two key aspects of metal – TMD contacts. First, we find that that a self-consistent model for charge transfer between the Bi and $MoSe_2$ can account for both the measured R_{sk}/R_{sh} ratio and its temperature dependence. The derived value of the band offset is very close to what would be expected from the Bi work function and $MoSe_2$ electron affinity. Second, we find that the measured value of the interfacial charge transfer rate is orders of magnitude below the prediction from density functional theory. This is consistent with previous studies; in fact, there is a longstanding discrepancy between measured values of specific contact resistivity and values predicted by *ab initio* theory. That discrepancy exists even in an ultraclean, well-characterized experimental

platform indicates that the problem likely lies with the theoretical approach, motivating further efforts in this direction. More broadly, the integrated approach demonstrated in this work can be readily expanded to other clean 2D semiconductors to allow better comparison between theory and experiment of the electrical contacts and transfer length dependencies on the doping level and temperature. However, there is still a challenge to predict the TMDs-metal scattering time from first principal calculations, a long-term problem recognized for van der Waals contacts. That is likely to be due to the momentum of Fermi surfaces and lattice constant mismatch in two materials. Therefore, in the presence of "hot spots" under the metal induced by the defects (internal defects inside the materials or external damages from the contact fabrication process) two effects can take place: 1) blocking the vertical current, and 2) relaxing momentum conservation restrictions by breaking translational symmetry. The two mechanisms affect the vertical transport in opposite directions and the optimal defect density, as well as the nature of the defects remains to be determined. Our analysis shows that the ultimate contact resistance of $R_{cf} = \sqrt{\rho_{\mathrm{cDFT}} R_{\mathrm{sh}}}$ =25 Ω μm could be reached by proper workfunction engineering to make $R_{\mathrm{sk}} = R_{\mathrm{sh}}$ and interface engineering by TMDC twisting and defect-engineering to reduce specific contact resistance to the theoretical limit of ρ_{cDFT} = 4 x 10^{-10} Ω cm^2.

Methods

High-purity $MoSe_2$ crystals were synthesized by a two-step self-flux process[22]. High-purity hBN bulk crystals were grown by Ni-Cr flux synthesis[42,43]. Monolayer and multilayer flakes of

these materials were exfoliated on 285-nm SiO_2. The heterostructure was assembled in a sequence of hBN/$MoSe_2$/etched hBN using a dry pick-up technique. SF_6 45 sccm gas with 15 W RF power and 45 mTorr gas pressure was used to etch out hBN in an Oxford Plasmalab 100 ICP-RIE instrument. The flipped heterostructure was treated using conventional electron-beam lithography, followed by electron-beam metal deposition of Bi/Au (60/60 nm) and a typical lift-off process. The electrical measurements were conducted in a vacuum probe station or temperature-controllable dry cryostat using a semiconductor parameter analyzer (Keysight B1500A). Raman spectra were taken with a Renishaw Raman system using a 532-nm laser source with a power of 1 mW and 10 s duration exposures. The AFM scans were done using a tapping mode in a Park Atomic Force Microscope. The cross-sectional sample was prepared by Thermofisher Scientific (TFS) Helios NanoLab 660 focused ion-beam (FIB/SEM), and the STEM images were taken using TFS Talos F200X TEM. STM and STS measurements were performed using a Scienta Omicron STM system at room temperature under an ultra-high vacuum (base pressure$<1.0\times10^{-10}$ torr).

Data Availability

The data supporting the plots within this paper and other study findings are available from the corresponding authors upon reasonable request.

Competing Interests Statement

The authors declare they have no competing interests.

ASSOCIATED CONTENT

Supporting Information.

AUTHOR INFORMATION

Corresponding Author

Email: liuyang.nano@gmail.com, vasilipe@buffalo.edu, jh2228@columbia.edu

Author Contributions

Y. L., V. P. and J. H. conceived the idea. Y. L., S. L., and Z. W. contributed equally to this work. Y. L. designed the experiment and did the electrical measurements, numerical calculations and data analysis, and Raman, PL, and SEM characterizations. S. L. and Z. W. performed heterostructure assembling and nanofabrication. S. L. and Y. L. grew s-TMDs and hBN crystals. S. L. did the STM and STS experiments. Z. W. developed the etching recipe for nano slits of hBN and carried out corresponding AFM characterization. A. H. M. A. and V. P. carried out *ab initio* calculations. V. P. developed the charge transfer model. A. Z. performed the cross-sectional STEM imaging. Y. L. V. P. and J. H. co-wrote the manuscript with inputs from all authors.

Funding Sources

Any funds used to support the research of the manuscript should be placed here (per journal style).

Notes

Any additional relevant notes should be placed here.

ACKNOWLEDGMENT

This work was primarily supported by the Department of Energy (DE-SC0016703). Synthesis of $MoSe_2$ and hBN was supported by the NSF MRSEC program at Columbia through the Center for Precision-Assembled Quantum Materials (DMR-2011738). Theoretical analysis of charge transfer was supported by the NSF DMR under award number 2235276. Y. L. thanks the support from National Natural Science Foundation of China (8206100616) and Beijing Natural Science Foundation (4242056).

REFERENCES

1 Manish Chhowalla, Debdeep Jena & Zhang, H. Two-dimensional semiconductors for transistors. *Nature Reviews Materials* **1**, 16052 (2016). https://doi.org:10.1038/natrevmats2016.52

2 Mak, K. F., Lee, C., Hone, J., Shan, J. & Heinz, T. F. Atomically thin MoS(2): a new direct-gap semiconductor. *Phys. Rev. Lett.* **105**, 136805 (2010). https://doi.org:10.1103/PhysRevLett.105.136805

3 Radisavljevic, B., Radenovic, A., Brivio, J., Giacometti, V. & Kis, A. Single-layer MoS2 transistors. *Nat. Nanotechnol.* **6**, 147-150 (2011). https://doi.org:10.1038/nnano.2010.279

4 Fuhrer, M. S. & Hone, J. Measurement of mobility in dual-gated MoS 2 transistors. *Nat. Nanotechnol.* **8**, 146-147 (2013).

5 Yoon, Y., Ganapathi, K. & Salahuddin, S. How good can monolayer MoS(2) transistors be? *Nano Lett.* **11**, 3768-3773 (2011). https://doi.org:10.1021/nl2018178

6 Liu, Y. *et al.* Promises and prospects of two-dimensional transistors. *Nature* **591**, 43-53 (2021). https://doi.org:10.1038/s41586-021-03339-z

7 Shen, P.-C. *et al.* Ultralow contact resistance between semimetal and monolayer semiconductors. *Nature* **593**, 211-217 (2021). https://doi.org:10.1038/s41586-021-03472-9

8 Li, W. *et al.* Approaching the quantum limit in two-dimensional semiconductor contacts. *Nature* **613**, 274-279 (2023). https://doi.org:10.1038/s41586-022-05431-4

9 Chou, A.-S. *et al.* in *2021 IEEE International Electron Devices Meeting (IEDM).* 7.2. 1-7.2. 4 (IEEE).

10 Wu, T. & Guo, J. Multiscale modeling of semimetal contact to two-dimensional transition metal dichalcogenide semiconductor. *Appl. Phys. Lett.* **121**, 023507 (2022).

11 Liu, Y., Huang, Y. & Duan, X. Van der Waals integration before and beyond two-dimensional materials. *Nature* **567**, 323 (2019).

12 Wang, Y. & Chhowalla, M. Making clean electrical contacts on 2D transition metal dichalcogenides. *Nature Reviews Physics* **4**, 101-112 (2021). https://doi.org:10.1038/s42254-021-00389-0

13 Yang, N. *et al.* Ab Initio Computational Screening and Performance Assessment of van der Waals and Semimetallic Contacts to Monolayer WSe $ _ {\text {2}} $ P-Type Field-Effect Transistors. *IEEE Trans. Electron Devices* (2023).

14 Kang, J., Liu, W., Sarkar, D., Jena, D. & Banerjee, K. Computational study of metal contacts to monolayer transition-metal dichalcogenide semiconductors. *Physical Review X* **4**, 031005 (2014).

15 Rhodes, D., Chae, S. H., Ribeiro-Palau, R. & Hone, J. Disorder in van der Waals heterostructures of 2D materials. *Nat. Mater.* **18**, 541-549 (2019).

16 Vancsó, P. *et al.* The intrinsic defect structure of exfoliated MoS2 single layers revealed by Scanning Tunneling Microscopy. *Scientific reports* **6**, 1-7 (2016).

17 Zhou, W. *et al.* Intrinsic structural defects in monolayer molybdenum disulfide. *Nano Lett.* **13**, 2615-2622 (2013).

18 Kim, C. *et al.* Fermi Level Pinning at Electrical Metal Contacts of Monolayer Molybdenum Dichalcogenides. *ACS Nano* **11**, 1588-1596 (2017). https://doi.org:10.1021/acsnano.6b07159

19 Liu, Y. *et al.* Approaching the Schottky–Mott limit in van der Waals metal–semiconductor junctions. *Nature* **557**, 696-700 (2018).

20 Liang, Q., Zhang, Q., Zhao, X., Liu, M. & Wee, A. T. Defect Engineering of Two-Dimensional Transition-Metal Dichalcogenides: Applications, Challenges, and Opportunities. *ACS Nano*

21 Tosun, M. *et al.* Air-stable n-doping of WSe2 by anion vacancy formation with mild plasma treatment. *ACS Nano* **10**, 6853-6860 (2016).

22 Song Liu *et al.* Two-step flux synthesis of ultrapure transition metal dichalcogenides. *ACS Nano* **17**, 16587–16596 (2023).

23 Liu, Y. *et al.* Low-resistance metal contacts to encapsulated semiconductor monolayers with long transfer length. *Nature Electronics* **5**, 579-585 (2022).

24 Klinger, M. More features, more tools, moreCrysTBox. *J. Appl. Crystallogr.* **50**, 1226-1234 (2017). https://doi.org:10.1107/s1600576717006793

25 Schroder, D. K. *Semiconductor material and device characterization*. (John Wiley & Sons, 2006).

26 Allain, A., Kang, J., Banerjee, K. & Kis, A. Electrical contacts to two-dimensional semiconductors. *Nat. Mater.* **14**, 1195 (2015).

27 Zhang, Q. *et al.* Bandgap renormalization and work function tuning in MoSe2/hBN/Ru (0001) heterostructures. *Nat. Commun.* **7**, 13843 (2016).

28 Faridi, A., Culcer, D. & Asgari, R. Quasiparticle band-gap renormalization in doped monolayer MoS 2. *Phys. Rev. B* **104**, 085432 (2021).

29 Chang, H. *et al.* Origin of phonon-limited mobility in two-dimensional metal dichalcogenides. *J. Phys.: Condens. Matter* **34**, 013003 (2021).

30 Zollner, K., Junior, P. E. F. & Fabian, J. Strain-tunable orbital, spin-orbit, and optical properties of monolayer transition-metal dichalcogenides. *Phys. Rev. B* **100**, 195126 (2019).

31 Khomyakov, P. A. *et al.* First-principles study of the interaction and charge transfer between graphene and metals. *Phys. Rev. B* **79** (2009). https://doi.org:10.1103/PhysRevB.79.195425

32 Zeng, J. *et al.* Ultralow contact resistance in organic transistors via orbital hybridization. *Nat. Commun.* **14**, 324 (2023).

33 Neaton, J. B., Hybertsen, M. S. & Louie, S. G. Renormalization of molecular electronic levels at metal-molecule interfaces. *Phys. Rev. Lett.* **97**, 216405 (2006).

34 Jupnik, H. Photoelectric Properties of Bismuth. *Physical Review* **60**, 884-889 (1941). https://doi.org:10.1103/PhysRev.60.884

35 Farmanbar, M. & Brocks, G. Ohmic Contacts to 2D Semiconductors through van der Waals Bonding. *Advanced Electronic Materials* **2** (2016). https://doi.org:10.1002/aelm.201500405

36 Perebeinos, V., Tersoff, J. & Haensch, W. Schottky-to-Ohmic crossover in carbon nanotube transistor contacts. *Phys. Rev. Lett.* **111**, 236802 (2013).

37 Datta, S. *Quantum transport: atom to transistor*. (Cambridge university press, 2005).

38 Xia, F., Perebeinos, V., Lin, Y. M., Wu, Y. & Avouris, P. The origins and limits of metal-graphene junction resistance. *Nat. Nanotechnol.* **6**, 179-184 (2011). https://doi.org:10.1038/nnano.2011.6

39 Nemec, N., Tománek, D. & Cuniberti, G. Contact Dependence of Carrier Injection in Carbon Nanotubes: AnAb InitioStudy. *Phys. Rev. Lett.* **96** (2006). https://doi.org:10.1103/PhysRevLett.96.076802

40 Kim, Y. *et al.* Breakdown of the interlayer coherence in twisted bilayer graphene. *Phys. Rev. Lett.* **110**, 096602 (2013).

41 Özçelik, V. O., Azadani, J. G., Yang, C., Koester, S. J. & Low, T. Band alignment of two-dimensional semiconductors for designing heterostructures with momentum space matching. *Phys. Rev. B* **94**, 035125 (2016).

42 Liu, S. *et al.* Single crystal growth of millimeter-sized monoisotopic hexagonal boron nitride. *Chem. Mater.* **30**, 6222-6225 (2018).

43 Onodera, M. *et al.* Hexagonal boron nitride synthesized at atmospheric pressure using metal alloy solvents: evaluation as a substrate for 2D materials. *Nano Lett.* **20**, 735-740 (2019).